

From χ EFT to Multi-Region Modeling: Neutron star structure with a polytropic extension of χ EFT and MUSES Calculation Engine multi-layer modeling

Federico Nola^{1, 2, 3}

¹*Dipartimento di Matematica e Fisica, Università degli Studi della Campania
“Luigi Vanvitelli”, viale Abramo Lincoln 5- I-81100 Caserta, Italy.*

²*Istituto Nazionale di Fisica Nucleare, Sezione di Napoli, Strada Comunale Cinthia, 80126 Napoli, Italy.*

³*Istituto Nazionale di Fisica Nucleare, Laboratori Nazionali di Frascati, C.P. 13, 00044 Frascati, Italy.*

(Dated: February 20, 2026)

Neutron stars provide a unique environment to probe the properties of dense nuclear matter. In this work, we present a comparative study between two approaches to modeling the neutron star structure: a Chiral Effective Field Theory based approach and the MUSES Calculation Engine framework, which uses three different approaches for the three density regions. We analyze the resulting mass-radius relations, discussing the respective advantages and limitations of the two methods.

I. INTRODUCTION

Neutron stars are objects representing the result of the collapse of a main-sequence star with mass $M_\star \sim 10M_\odot$ and $R_\star \sim 5R_\odot$. The result of this process is an object with radius $R \sim 10 - 13$ km and mass $M \sim 1.1 - 2.4 M_\odot$, making neutron stars extremely dense astrophysical objects capable of significantly distorting the local spacetime. The mean density of a neutron star is $\bar{\rho} \sim 10^{15}$ g cm⁻³, which is comparable to the density inside the atomic nuclei. Moreover, they have strong magnetic fields $B \sim 10^8 - 10^{15}$ G. The matter is compressed into such a small volume that its behavior is completely defined by quantum mechanical effects. How the matter responds to this extreme squeezing, as the particles try to counter the compressing force, is described in the Equation of State (EoS) of cold and dense matter, which is still unknown.

In recent years, substantial advancements have been made in constraining the nuclear EoS through both theoretical developments and multimessenger astrophysical observations. Observational data from gravitational wave events (e.g., GW170817) [1], pulsar timing (e.g., PSR J0740+6620) [2], and X-ray measurements (e.g., NICER) [3] have imposed increasingly stringent constraints on the mass-radius relation of neutron stars.

The study of the equations of state for neutron stars is still a very hot topic in physics. Nuclear interactions derived from Chiral Effective Field Theory (χ EFT) provide a solid starting point to describe nuclear forces, including the essential role of three-body interactions. Starting from this QCD-based framework, it has been possible to develop several methods for the construction of an equation of state capable of reproducing observables consistent with observational data.

This paper presents two different methods for constructing the equation of state for neutron stars. On

one hand, a β -stabilized χ EFT Equation of State [4] is obtained from a purely χ EFT approach, where the interactions present inside the neutron star are of a purely nuclear nature. On the other hand, MUSES Calculation Engine [5, 6] represents a complete tool for the construction of an Equation of State for neutron stars, in which the microphysics of the layers at different densities is properly diversified. The great versatility of this tool in the construction of equations of state allows for the study of physical phenomena that depend on such EoSs. Using MUSES Calculation Engine, a paper linking the neutron star Equation of State to axions is in preparation [7].

In section II, this work provides a description of these two methods used, both starting from the same chiral potential. The results are shown in Section III.

II. MODELING METHODS

A. β -stabilized χ EFT Equation of State & piecewise polytropic extension

Chiral Effective Field theory provides a controlled and largely model-independent description of nuclear interactions at low energies. It is constructed from the most general effective Lagrangian consistent with the symmetries of low-energy QCD, in particular spontaneously broken chiral symmetry, with nucleons and pions as the relevant degrees of freedom. The long-range part of the interaction is governed by pion exchange, while unresolved short-distance physics is encoded in contact operators. Schematically,

$$\mathcal{L}_{\text{eff}} = \mathcal{L}_{\pi\pi} + \mathcal{L}_{\pi N} + \mathcal{L}_{NN} + \dots, \quad (1)$$

where $\mathcal{L}_{\pi\pi}$ describes pion dynamics, $\mathcal{L}_{\pi N}$ pion-nucleon couplings, and \mathcal{L}_{NN} short-range nucleon-nucleon interactions.

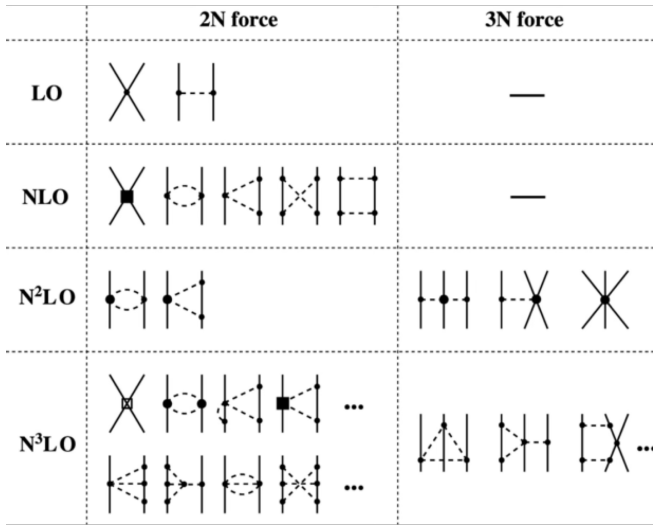


FIG. 1. Hierarchy of chiral nuclear interactions up to fourth order (or N^3LO) in the chiral expansion. Nucleons (pions) are represented by solid (dashed) lines. The circled numbers indicate the number of short-range contact low-energy constants. Note that there is a finite number of diagrams at each order in the chiral power counting expansion.

The expansion is organized by a separation of scales between a soft scale $q \sim m_\pi$ and a hard breakdown scale $\Lambda_\chi \sim 1 \text{ GeV}$, leading to an ordering in powers of $Q \equiv q/\Lambda_\chi$. Using Weinberg power counting, an irreducible diagram is assigned a chiral index

$$\nu = -2 + 2A - 2C + 2L + \sum_i \Delta_i, \quad (2)$$

with A the number of nucleons, C the number of connected pieces, L the number of loops, and

$$\Delta_i \equiv d_i + \frac{n_i}{2} - 2, \quad (3)$$

where d_i counts derivatives (or pion-mass insertions) and n_i the number of nucleon fields at vertex i . This ordering generates the characteristic hierarchy of two- and many-nucleon forces (Fig. 1).

Neutron star EoS can be built starting from a χ EFT approach, to describe the inner crust and the core, combined with the Negele-Vautherin and Baym-Pethick-Sutherland model [8, 9], which describes the stellar crust for a baryon density $n \leq 0.08 \text{ fm}^{-3}$.

In this article, we used an approach inspired by a previous work from Bombaci and Logoteta [4], which uses a new EoS for asymmetric β -stable nuclear matter to compute various structural properties of non-rotating neutron stars. The basic ingredients are the EoSs for Pure Neutron Matter (PNM), $\beta = 1$, and Symmetric Nuclear Matter (SNM), $\beta = 0$. In this paper, they are calculated through Goldstone Perturbation series [10].

In the Goldstone formalism, the energy density E of interacting nuclear matter is obtained from a perturba-

tive expansion of the Hamiltonian $\mathcal{H} = \mathcal{H}_0 + \lambda \mathcal{V}$ [11], with $\mathcal{V} = \mathcal{V}_{NN} + \mathcal{V}_{3N}$ and λ a book-keeping parameter,

$$E(k_F^p, k_F^n) = E_0(k_F^p, k_F^n) + \lambda E_1(k_F^p, k_F^n) + \quad (4)$$

$$+ \lambda^2 E_2(k_F^p, k_F^n) + \mathcal{O}(\lambda^3). \quad (5)$$

Here E_0 is the free Fermi-gas contribution, while E_1 and E_2 correspond to antisymmetrized Goldstone diagrams (Hartree-Fock and second order) [11, 12]. In the χ EFT context, the use of softened low-momentum interactions and Pauli blocking typically improves the convergence of the expansion, making many-body perturbation theory viable in nuclear matter [13]. At $T = 0$, the energy density coincides with the free-energy density, $F(n_B, \delta, T = 0) = E$, with $n_B = n_n + n_p$ and $\delta = (n_n - n_p)/(n_n + n_p)$ [14, 15].

The first-order (Hartree-Fock) term can be written as

$$E_1 = \frac{1}{2} \text{tr}_{\sigma_1 \tau_1} \text{tr}_{\sigma_2 \tau_2} \int \frac{d^3 k_1}{(2\pi)^3} \int \frac{d^3 k_2}{(2\pi)^3} n_{k_1} n_{k_2} \langle \mathbf{12} | \bar{V} | \mathbf{12} \rangle, \quad (6)$$

where $n_k \equiv n_k^\tau$ are occupation numbers and \bar{V} is the antisymmetrized interaction; in practical χ EFT applications, three-nucleon forces are often incorporated via an effective density-dependent two-body interaction [12]. The second-order contribution involves intermediate particle-particle and hole-hole states,

$$E_2 = -\frac{1}{8} \left(\prod_{i=1}^4 \text{tr}_{\sigma_i \tau_i} \int \frac{d^3 k_i}{(2\pi)^3} \right) \cdot (2\pi)^3 \delta(\vec{k}_1 + \vec{k}_2 - \vec{k}_3 - \vec{k}_4) \cdot \frac{n_1 n_2 \bar{n}_3 \bar{n}_4 - \bar{n}_1 \bar{n}_2 n_3 n_4}{\varepsilon_3 + \varepsilon_4 - \varepsilon_1 - \varepsilon_2} |\langle \mathbf{12} | \bar{V} | \mathbf{34} \rangle|^2, \quad (7)$$

with $\bar{n} = 1 - n$ and $\varepsilon_k \equiv \varepsilon_k^\tau$ the single-particle spectrum entering the energy denominator, typically including a self-energy contribution $U(k)$ [13, 14].

To obtain the PNM and SNM EoSs, we employ a charge-dependent two-nucleon interaction constructed up to N^3LO in the chiral expansion, with long-range one-/multi-pion-exchange contributions and short-range contact operators fitted in a partial-wave representation [16, 17]. High-momentum components are suppressed by a smooth non-local regulator

$$f(p', p) = \exp \left[- \left(\frac{p}{\Lambda} \right)^{2n} - \left(\frac{p'}{\Lambda} \right)^{2n} \right], \quad (8)$$

with cutoff $\Lambda = 450 \text{ MeV}$ and exponent $n = 3$. Three-nucleon forces are included consistently at N^2LO , with a 3N regulator scale $\Lambda_{3N} = 700 \text{ MeV}$ and low-energy constants $c_D = -0.24$, $c_E = -0.106$ (in addition to the long-range 2π -exchange piece fixed by the πN LECs c_{1-4}). In the many-body calculation, the 3N interaction is implemented through the normal-ordered, density-dependent in-medium two-body interaction $V_{NN}^{\text{med}}(p', p; n_p, n_n)$, obtained by summing one nucleon over the filled Fermi sea,

and combined with the free-space V_{NN} in the Many-Body Perturbation Theory (MBPT) expansion [18, 19].

It is essential that these EoSs contain the 3-body contribution, as it has been shown that a 2-body approach does not provide the right density and pressure profiles for the construction of a neutron star model. The EoS for asymmetric nuclear matter can be calculated numerically by solving the generalized Bethe-Goldstone equations for various values of the asymmetry parameter β ($0 \leq \beta \leq 1$) and various densities n .

The next step consists of β -stabilizing the asymmetric-matter results, density by density. For each value of the baryon number density $n \equiv n_B$ (with $n_B = n_n + n_p$, where n_n and n_p are the neutron and proton number densities), we impose charge neutrality by solving the coupled conditions $\mu_n - \mu_p = \mu_e$, and $\mu_e = \mu_\mu$ when muons are present, together with $n_p = n_e + n_\mu$, $\mu_\nu = 0$. Here μ_i denotes the chemical potential of species $i \in \{n, p, e, \mu, \nu\}$, defined at zero temperature as $\mu_i = \frac{\partial \varepsilon}{\partial n_i}$ (with ε the total energy density). The condition $\mu_n - \mu_p = \mu_e$ enforces β -equilibrium for the process $n \leftrightarrow p + e^- + \bar{\nu}_e$ in neutrino-free matter, while $\mu_e = \mu_\mu$ accounts for equilibrium under $e^- \leftrightarrow \mu^- + \nu_e + \bar{\nu}_\mu$ once the electron chemical potential exceeds the muon rest mass and muons can appear. Charge neutrality requires that the positive proton charge density n_p is balanced by the total negative lepton charge density $n_e + n_\mu$, where n_e and n_μ are the electron and muon number densities. Finally, $\mu_\nu = 0$ expresses the assumption of cold, catalyzed matter in which neutrinos freely escape. Electrons and muons treated as free relativistic Fermi gases. These constraints fix the proton fraction $x_p(n)$ and lepton densities, from which we compute the EoS $(\varepsilon(n), P(n))$ for β -stable matter. Full details of the calculation can be found in [4].

A purely χ EFT equation of state cannot be safely used over the entire density range explored in neutron star interiors, since χ EFT is constructed as a low-momentum expansion in the dimensionless parameter

$$Q \sim \frac{\max\{k_F, m_\pi\}}{\Lambda_\chi},$$

where k_F is a typical Fermi momentum and Λ_χ is the breakdown scale of the theory [20–22]. As the density increases, $k_F \propto n^{1/3}$ grows, and the expansion parameter Q approaches unity. In this regime, the chiral expansion converges slowly: the spread between different chiral orders significantly increases, regulator artifacts become more pronounced, and contributions from higher-order 3N and 4N forces are no longer guaranteed to be small [21, 22]. Moreover, at several times nuclear saturation density the system approaches scales where non-nucleonic degrees of freedom (hyperons, Δ -isobars, deconfined quarks) and possible phase transitions may become relevant, so that no purely hadronic EFT can be

regarded as quantitatively reliable on its own [23, 24]. For these reasons, modern microscopic EoS calculations based on chiral forces are typically considered robust only up to $n \lesssim 0.3\text{--}0.4 \text{ fm}^{-3}$; at higher densities, the χ EFT segment is used as a microscopic anchor and is matched to a controlled high-density extension constrained by causality.

In this work, the high-density continuation follows the strategy proposed by Sammarruca and Ajagbonna [25], and is implemented by matching the microscopic β -stable χ EFT EoS to a *single* stiff polytropic segment, followed by a *speed-of-sound* (SoS) extension at the highest densities. Here n denotes the baryon density (in fm^{-3}), and the microscopic χ EFT EoS is used up to the first matching density n_1 . For $n_1 \leq n \leq n_2$, we adopt a polytropic form [4]

$$P(n) = \alpha_1 \left(\frac{n}{n_0} \right)^{\Gamma_1}, \quad (9)$$

and obtain the corresponding energy density from thermodynamic consistency at $T = 0$, $P(n) = n^2 \frac{d(\varepsilon/n)}{dn}$, namely

$$\varepsilon(n) = \frac{\alpha_1}{\Gamma_1 - 1} \left(\frac{n}{n_0} \right)^{\Gamma_1} + c_1 n. \quad (10)$$

The constants α_1 and c_1 are fixed by enforcing continuity of both P and ε at n_1 , i.e. $P(n_1) = P_{\chi\text{EFT}}(n_1)$ and $\varepsilon(n_1) = \varepsilon_{\chi\text{EFT}}(n_1)$.

For $n \geq n_2$ we switch to a causality-controlled extension by parametrizing the squared sound speed $v_s^2(n) \equiv \frac{dP}{d\varepsilon}$ as [25]

$$v_s^2(n) = 1 - a \exp \left[-\frac{(n - n_c)^2}{w^2} \right], \quad (11)$$

where the parameters (a, n_c) are determined by matching v_s^2 and its derivative $\frac{dv_s^2}{dn}$. The matching value $v_s^2(n_2)$ is computed from the polytrope through

$$v_s^2(n) = \frac{dP/dn}{d\varepsilon/dn}, \quad (12)$$

$$\frac{dP}{dn} = \Gamma_1 \frac{P}{n}, \quad (13)$$

$$\frac{d\varepsilon}{dn} = \frac{\Gamma_1}{\Gamma_1 - 1} \frac{P}{n} + c_1, \quad (14)$$

and $\frac{dv_s^2}{dn} \Big|_{n_2}$ is evaluated numerically by a symmetric finite difference.

In addition, a phenomenological upper cap is enforced,

$$0 < v_s^2(n) \leq v_{s,\text{cap}}^2 < 1, \quad v_{s,\text{cap}}^2 \geq v_s^2(n_2), \quad (15)$$

so that stability and causality are satisfied by construction and the EoS is not artificially softened immediately above the matching point. Given $v_s^2(n)$, the SoS branch is reconstructed by integrating the thermodynamically consistent relations

$$\frac{d\varepsilon}{dn} = \frac{\varepsilon + P}{n}, \quad (16)$$

$$\frac{dP}{dn} = v_s^2(n) \frac{d\varepsilon}{dn} = v_s^2(n) \frac{\varepsilon + P}{n}, \quad (17)$$

starting from the matched values $(\varepsilon(n_2), P(n_2))$. Contrary to a fixed-density truncation, in our implementation the SoS integration is stopped *dynamically*, i.e. we integrate until the SoS profile reaches its high-density plateau,

$$|v_s^2(n) - v_{s,\text{cap}}^2| < \delta_{\text{pl}}, \quad \delta_{\text{pl}} \ll 1, \quad (18)$$

after which the continuation becomes effectively constant- v_s^2 .

The final composite EoS is therefore: χEFT ($n \leq n_1$) + polytrope ($n_{1,2}$) + SoS (n_2).

Later in this paper, we will refer to the EoS obtained with this method as **P χ EFT-npe μ** .

Before solving the Tolman-Oppenheimer-Volkoff (TOV) equations [26], we verify causality and stability by checking that the reconstructed β -stable EoS satisfies

$$0 < v_s^2(n) = \frac{dP}{d\varepsilon} \leq 1. \quad (19)$$

In practice, this is ensured by construction through the cap (15), while additional numerical checks are performed on the final tabulated $P(\varepsilon)$.

A low-density crust EoS [8, 9] is attached to the β -stable extended EoS at the minimum tabulated pressure P_0 . Since the TOV system requires $\varepsilon(P)$, the composite table is cast into a globally defined function $\varepsilon(P)$: inside the tabulated domain we use a monotone interpolation $\varepsilon_{\text{tab}}(P)$, while outside we adopt analytic continuations. At low pressures $P < P_0$ we attach a crust polytrope,

$$\varepsilon(P) = \left(\frac{P}{K_{\text{crust}}} \right)^{1/\gamma_{\text{crust}}}, \quad K_{\text{crust}} = \frac{P_0}{\varepsilon_0^{\gamma_{\text{crust}}}}, \quad (20)$$

with (P_0, ε_0) the first tabulated point. At high pressures, above the last tabulated point (ε_*, P_*) , we employ a causal linear continuation consistent with the asymptotic constant- v_s^2 regime,

$$\varepsilon(P) = \varepsilon_* + \frac{P - P_*}{v_{s,\text{cap}}^2} \quad \leftrightarrow \quad P(\varepsilon) = P_* + v_{s,\text{cap}}^2 (\varepsilon - \varepsilon_*), \quad (21)$$

which preserves $0 < v_{s,\text{cap}}^2 \leq 1$ by construction and allows the stellar solver to explore central pressures beyond the tabulated range.

With $\varepsilon(P)$ specified for all $P > 0$, we solve the TOV equations [26]

$$\frac{dP}{dr} = - \frac{[\varepsilon(P) + P][m(r) + 4\pi r^3 P]}{r[r - 2m(r)]}, \quad (22)$$

$$\frac{dm}{dr} = 4\pi r^2 \varepsilon(P), \quad (23)$$

starting from a small radius r_0 to avoid the coordinate singularity at $r = 0$, with initial mass $m(r_0) = \frac{4\pi}{3} r_0^3 \varepsilon(P_c)$ for a given central pressure P_c . The stellar radius R is defined by the first root of $P(R) = P_{\text{surf}}$, where P_{surf} is taken to be a very small pressure (typically $P_{\text{surf}} \ll P_0$), and the gravitational mass is $M = m(R)$. By scanning over P_c one obtains the full mass-radius sequence, which can be compared with observational constraints.

B. MUSES Calculation Engine Nuclear Equation of State

MUSES Calculation Engine (MUSES CE) [5, 6] is a composable workflow management system that performs calculations of the EoSs by combining algorithms from three different models that are valid in complementary density regimes.

At low densities, the *Crust Density Functional theory* (Crust-DFT) is employed as a phenomenological approach describing nuclei in equilibrium with neutrons and protons in a low-temperature T regime. This module is based on the work of Lim and Holt [27]. Here, the authors construct a set of extended Skyrme mean-field functionals ($Sk\chi 414/450/500$) that are simultaneously constrained by the bulk equation of state from χEFT and by the ground-state energies of doubly magic nuclei, and then use these calibrated models to study the structure of neutron stars with particular emphasis on the crust and the crust–core boundary. The crust is obtained within a Wigner–Seitz (WS) cell framework using complementary levels of sophistication. The crust–core transition density is then identified by comparing the energy density of this inhomogeneous WS configuration with that of uniform β -equilibrated matter, yielding relatively low transition densities and illustrating the strong sensitivity to the adopted nuclear mass model. This strategy is intrinsically reliable only for the outer crust, because in the inner crust the neutron chemical potential becomes positive and a free neutron gas must be treated self-consistently. A realistic inner-crust description is achieved with a compressible liquid-drop model (CLDM) in which the total energy density includes bulk, surface, Coulomb, and neutron-gas contributions. By minimizing the energy for different geometries, it is possible to determine both the energetically favored pasta sequence and the transition to uniform matter. The crust–core boundary is validated using a thermodynamic instability criterion against density fluctuations, which connects the transition density

to derivatives of the neutron/proton chemical potentials and to the Skyrme gradient coefficients.

Around saturation density, MUSES CE involves the use of χ EFT, which provides a model-independent framework to study strongly interacting matter at the characteristic energy scales of nuclei.

Beyond saturation density, the *Chiral Mean Field* (CMF) model is used; it is based on a non-linear realization of the $SU(3)$ sigma model, where hadronic interactions are mediated by meson exchange (including σ , ζ , δ , ϕ and n). Cruz-Camacho et al. [28] present a major numerical and software-development update of the CMF framework by introducing CMF++, a modular, optimized C++ reimplementation that is designed to explore dense QCD matter over a three-dimensional chemical-potential space, spanned by the baryon, electric-charge, and strangeness chemical potentials. The work focuses on zero temperature and systematically maps the regions of stable, metastable, and unstable solutions associated with vacuum, hadronic, and quark degrees of freedom, quantifying how phase boundaries and the nature of phase conversion depend on the independent variation of chemical potentials. A key result enabled by the drastic speedup is the first practical extraction of high-order susceptibilities within this CMF setup, which the authors use to characterize the deconfinement sector and to identify multiple distinct regimes, including a light hadronic phase, a strangeness-dominated hadronic phase, and quark deconfinement, connected through phase transitions of different orders and featuring critical structures such as a tricritical point. In practice, CMF++ provides the uniform-matter EOS appropriate for the core and for phase-transition studies, and a realistic stellar model would attach this high-density EOS to a dedicated crust prescription at low densities. In addition to reproducing key QCD features, the CMF model is fully relativistic and therefore respects causality.

Fig. 2 shows an example of a non-rotating neutron star slice calculated through MUSES CE. The size of each layer strongly depends on the maximum central density, which in turn produces a given mass and radius of the star. This means that heavier neutron stars have larger contributions from the core.

For the complete description of a neutron star, three additional modules are employed.

The *lepton module* adds the lepton contribution to each EoS, ensuring charge neutrality and, in principle, β -equilibrium. The *synthesis module* is then used to obtain a single, unified EoS describing the neutron star structure, by matching the three underlying EoSs through appropriate thermodynamic variables. Finally, the *QLIMR module* is a full general-relativity solver used to compute global neutron-star observables within the Hartle-Thorne slow-rotation scheme [29, 30].

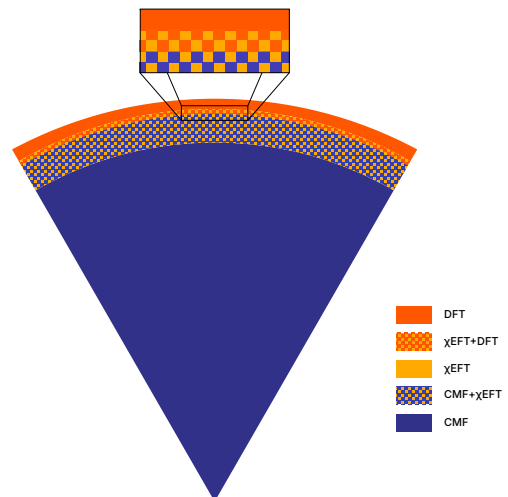


FIG. 2. Example of neutron star slice obtained with MUSES CE [5]. The different colors indicate the different models used, as shown in the legend. The proportions of the layers depend on the mass of the star.

MUSES CE therefore allows us to construct a complete, high-precision model of a neutron star, explicitly accounting for the different physical nature of the various layers that compose it.

For the purpose of this article, the CMF module has been set to reproduce an EoS of nuclear matter with C4 coupling scheme [28], having consistency in the composition of the modeled core via β -stable extended χ EFT EoS. This means that the baryonic contribution comes only from neutrons and protons and the leptonic contribution is given by electrons, throughout the star, and muons, above a certain density threshold compatible with β -equilibrium and charge neutrality. The synthesis between the modules, moreover, was performed via hyperbolic tangent.

We will refer to the EoS obtained with this method as **MUSES-*npeμ***.

III. RESULTS AND CONCLUSIONS

In this work we have constructed and compared two high-density continuation strategies for a cold, β -stable $npe\mu$ equation of state, and solved the stellar structure equations to obtain the corresponding neutron-star mass-radius ($M - R$) relations. In both cases, the core description was intentionally restricted to nucleonic degrees of freedom only, in order to isolate in a controlled manner the impact of the high-density modeling on macroscopic observables.

In this section, we present the results obtained for this analysis, comparing them with constraints on the EoS

| | |
|----------------------|------------------------|
| n_1 | 0.35 fm^{-3} |
| n_2 | 0.64 fm^{-3} |
| Γ_1 | 3.45 |
| w | 0.55 fm^{-3} |
| $v_{s,\text{cap}}^2$ | 0.80 |

| | |
|------------|--------|
| α_1 | 1.36 |
| c_1 | 954.30 |
| a | 3.45 |
| n_c | 0.21 |

TABLE I. On the left: computational parameters required as input for extensions of the equation of state. On the right: numerical parameters obtained to ensure continuity.

| | Mass [M_\odot] | Radius [km] |
|--------------------------|--------------------|-------------|
| $P\chi\text{EFT-}npe\mu$ | 2.17 | 10.13 |
| $\text{MUSES-}npe\mu$ | 2.04 | 11.3 |

TABLE II. Summary table of mass and radius results obtained with $P\chi\text{EFT-}npe\mu$ and $\text{MUSES-}npe\mu$.

for non-rotating neutron stars, presented in Miller and Coleman's paper [31]. These constraints are obtained by statistical analysis combining observational data from pulsars and LIGO/VIRGO, with their EoS obtained by Gaussian Processes. For a detailed description of the calculation, please refer to their paper [31].

Fig. 3 shows the EoSs obtained for the two approaches just described. The EoS from $P\chi\text{EFT-}npe\mu$ approach is obtained using the numerical parameters shown in Tab. I. The dependence on these expansion parameters is commented in Appendix A. Details on the dependence on computational and Synthesis parameters of the $\text{MUSES-}npe\mu$ equation of state are described in [5].

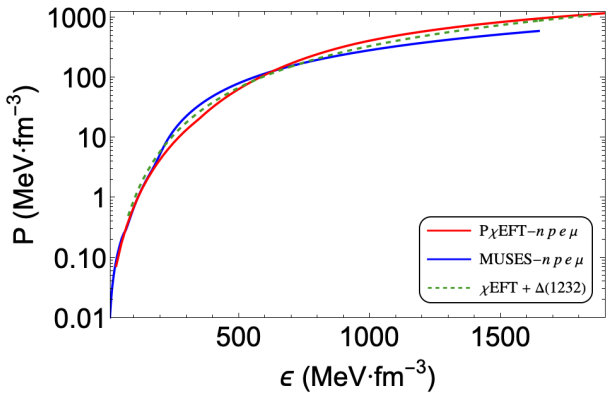


FIG. 3. EoS from $P\chi\text{EFT-}npe\mu$ and $\text{MUSES-}npe\mu$ [6]. Solid lines represent the results obtained from the analyses performed in this paper, with the two different approaches. The dashed line represent the results in [4], obtained with a $\chi\text{EFT} + \Delta(1232)$ approach.

Table II shows the results obtained with the two methods considered in this paper.

The comparison plot of the two $M - R$ curves is shown in Fig. 4; the obtained curves are compared with

the results obtained by two other purely microscopic approaches, one using an χEFT model including the $\Delta(1232)$ isobar intermediate state [4] and the other a DDFGOS(APR) with unified crust model [32]. All these results are compared with the confidence region calculated in [31].

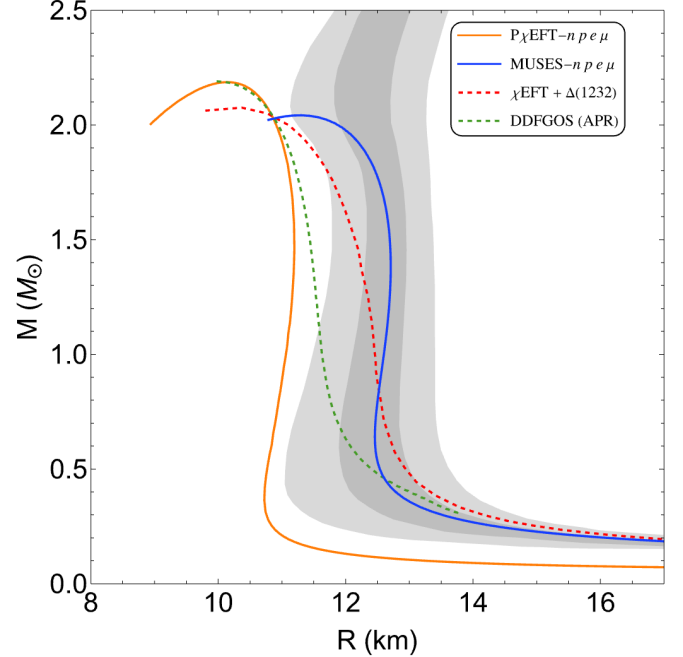


FIG. 4. $M - R$ relation from $P\chi\text{EFT-}npe\mu$ and $\text{MUSES-}npe\mu$ [6]. Solid lines represent the results obtained from the analyses performed in this paper, with the two different approaches. Dashed lines represent the results for two other different microscopic approaches [4, 32]. In light (dark) grey the 50% (90%) confidence region for neutron star $M - R$ relation shown in [31].

The two EoS are mutually consistent in the density domain where the microscopic input is expected to be most reliable, while they exhibit noticeable differences at higher densities, where the stiffness of the EoS becomes the key driver of both the maximum supported mass and stellar compactness. $P\chi\text{EFT-}npe\mu$ produces more compact configurations and supports a larger maximum mass (approximately $M_{\text{max}} \simeq 2.17 M_\odot$ with a characteristic radius $R(M_{\text{max}}) \simeq 10.13 \text{ km}$), whereas the $\text{MUSES-}npe\mu$ construction yields slightly lower maximum masses and larger radii (approximately $M_{\text{max}} \simeq 2.04 M_\odot$ and $R(M_{\text{max}}) \simeq 11.3 \text{ km}$). This complementarity highlights that, at fixed composition, the dominant source of uncertainty in global stellar properties arises from the treatment of the high-density regime.

In conclusion, our results indicate that neither approach is *universally* superior. The polytropic continuation is a flexible and economical way to bracket the im-

pact of high-density stiffness while preserving a controlled match to the underlying χ EFT input; however, its predictive power at the highest densities is intrinsically limited by the fact that it is a parametrized extrapolation, whose stiffness is directly driven by the chosen adiabatic index and matching conditions. Conversely, MUSES CE provides a more physically grounded route to the high-density regime: rather than extrapolating χ EFT with an ad hoc polytrope, it embeds the core in a microphysics-motivated framework in which the behavior of $P(\varepsilon)$ and the evolution of the sound speed can be controlled in a manner that remains causal to substantially higher energy densities. For this reason, if one emphasizes *physical realism* in the extrapolation to supranuclear densities, MUSES CE offers a more credible description of the deep core than a purely polytropic extension of χ EFT.

At the same time, the two strategies should be viewed as complementary. The polytropic continuation is particularly useful as a diagnostic tool to quantify how strongly global stellar properties depend on the assumed stiffness above the microscopic domain, and to identify parameter regions where causality becomes restrictive. MUSES CE, instead, is well suited for systematic high-density studies in which the composition of the core is varied in a controlled way. In particular, it can be straightforwardly employed to investigate scenarios beyond a purely nucleonic core, including the appearance of additional baryonic degrees of freedom and/or a transition to deconfined matter (e.g., quarks), as motivated by the underlying references and model extensions. This makes MUSES CE a natural platform for exploring hybrid-star phenomenology and for assessing the interplay between composition-driven softening/stiffening mechanisms and observational constraints.

Ultimately, discriminating quantitatively between high-density continuations requires going beyond a comparison of $M - R$ curves alone. A decisive assessment will rely on the combined enforcement of multi-messenger constraints and on testing the robustness of the conclu-

sions when additional high-density degrees of freedom are introduced. Within this broader program, our nucleonic-core results provide a consistent baseline and clarify the respective roles of (i) purely parametric extrapolations anchored to χ EFT and (ii) microphysics-based high-density frameworks capable of addressing both causality and composition in a unified manner.

The presence of a large number of modifiable computational parameters – corresponding to different behaviors, interactions, and particles in the neutron star – makes MUSES CE a very versatile tool for testing different theories for the neutron star core, allowing us to generate EoSs with different core properties, selecting the desired interactions and particles. A prominent example relevant from particle phenomenology is the bound on axion-nucleon coupling obtained from neutron star cooling [33], where the EoS is a fundamental ingredient. A paper on neutron star cooling limit on axions is currently in preparation [7].

ACKNOWLEDGMENTS

I acknowledge the use of the MUSES Calculation Engine for the neutron star structure calculations performed in this work. I also thank the MUSES CE developers and community for their helpful feedback and support through the official forum.

I would like to thank my supervisor, Nunzio Itaco, for their invaluable support and guidance throughout the writing of this paper, as well as for their helpful feedback and suggestions that significantly improved the manuscript.

Finally, I am grateful to Fernando Arias Aragón for valuable discussions and contributions that helped refine the construction of the equation of state used in this study.

[1] B. P. Abbott, R. Abbott, T. Abbott, F. Acernese, K. Ackley, C. Adams, T. Adams, P. Addesso, R. Adhikari, V. Adya *et al.*, “Gravitational waves and gamma-rays from a binary neutron star merger: Gw170817 and grb 170817a,” *The Astrophysical Journal Letters*, vol. 848, no. 2, p. L13, 2017.

[2] T. E. Riley, A. L. Watts, P. S. Ray, S. Bogdanov, S. Guillot, S. M. Morsink, A. V. Bilous, Z. Arzoumanian, D. Choudhury, J. S. Deneva *et al.*, “A nicer view of the massive pulsar psr j0740+ 6620 informed by radio timing and xmm-newton spectroscopy,” *The Astrophysical Journal Letters*, vol. 918, no. 2, p. L27, 2021.

[3] K. C. Gendreau, Z. Arzoumanian, and T. Okajima, “The neutron star interior composition explorer (nicer): an explorer mission of opportunity for soft x-ray timing spectroscopy,” in *Space telescopes and instrumentation 2012: ultraviolet to gamma ray*, vol. 8443. SPIE, 2012, pp. 322–329.

[4] I. Bombaci and D. Logoteta, “Equation of state of dense nuclear matter and neutron star structure from nuclear chiral interactions,” *Astronomy & Astrophysics*, vol. 609, p. A128, 2018.

[5] M. R. Pelicer, N. Cruz-Camacho, C. Conde-Ocacionez, D. Friedenberg, S. Roy, Z. Zhang, T. A. Manning, M. G. Alford, A. Clevinger, J. Grefa, R. Haas, A. Haber, M. Hippert, J. W. Holt, J. Jahan, M. Kahangirwe, R. Kumar, J. Peterson, H. Shah, A. W. Steiner, H. Tan, Y. Yang, V. Vovchenko, V. Dexheimer, J. Noronha, J. Noronha-Hostler, C. Ratti, and N. Yunes, “Building neutron stars with the muses calculation engine,” *Phys. Rev. D*, vol. 111, p. 103037, May 2025. [Online]. Available: <https://link.aps.org/doi/10.1103/PhysRevD.111.103037>

[6] T. A. Manning, “Muses calculation engine,” 2 2025. [Online]. Available: <https://musesframework.io>

[7] F. Nola and F. Arias Aragón, “Revisiting the neutron star cooling limit on axions with muses calculation engine,” 2026, in preparation.

[8] J. W. Negele and D. Vautherin, “Neutron star matter at sub-nuclear densities,” *Nuclear Physics A*, vol. 207, no. 2, pp. 298–320, 1973.

[9] G. Baym, H. A. Bethe, and C. J. Pethick, “Neutron star matter,” *Nuclear Physics A*, vol. 175, no. 2, pp. 225–271, 1971.

[10] K. A. Brueckner and J. L. Gammel, “Properties of nuclear matter,” *Phys. Rev.*, vol. 109, pp. 1023–1039, Feb 1958. [Online]. Available: <https://link.aps.org/doi/10.1103/PhysRev.109.1023>

[11] ———, “Properties of nuclear matter,” *Phys. Rev.*, vol. 109, p. 1023, 1958.

[12] L. Coraggio, J. W. Holt, N. Itaco, R. Machleidt, L. E. Marcucci, and F. Sammarruca, “Nuclear-matter equation of state with consistent two- and three-body perturbative chiral interactions,” *Phys. Rev. C*, vol. 89, p. 044321, 2014.

[13] S. K. Bogner, A. Schwenk, R. J. Furnstahl, and A. Nogga, “Is nuclear matter perturbative with low-momentum interactions?” *Nucl. Phys. A*, vol. 763, p. 59, 2005.

[14] C. Wellenhofer, J. W. Holt, N. Kaiser, and W. Weise, *Phys. Rev. C*, vol. 89, p. 064009, 2014.

[15] C. Wellenhofer, J. W. Holt, and N. Kaiser, “Divergence of the isospin-asymmetry expansion of the nuclear equation of state in many-body perturbation theory,” *Phys. Rev. C*, vol. 93, p. 055802, 2016.

[16] D. Entem and R. Machleidt, “Accurate charge-dependent nucleon-nucleon potential at fourth order of chiral perturbation theory,” *Phys. Rev. C*, vol. 68, p. 041001, 2003.

[17] R. Machleidt and D. Entem, “Chiral effective field theory and nuclear forces,” *Phys. Rep.*, vol. 503, pp. 1–75, 2011.

[18] J. Holt, N. Kaiser, and W. Weise, “Chiral three-nucleon interaction and the 14c-dating β decay,” *Phys. Rev. C*, vol. 79, p. 054331, 2009.

[19] ———, “Density-dependent effective nucleon-nucleon interaction from chiral three-nucleon forces,” *Phys. Rev. C*, vol. 81, p. 024002, 2010.

[20] E. Epelbaum, H.-W. Hammer, and U.-G. Meißner, “Modern theory of nuclear forces,” *Reviews of Modern Physics*, vol. 81, no. 4, pp. 1773–1825, 2009.

[21] R. Machleidt and D. R. Entem, “Chiral effective field theory and nuclear forces,” *Physics Reports*, vol. 503, no. 1, pp. 1–75, 2011.

[22] C. Drischler, J. Holt, and C. Wellenhofer, “Chiral effective field theory and the high-density nuclear equation of state,” *Annual Review of Nuclear and Particle Science*, vol. 71, no. 1, pp. 403–432, 2021.

[23] M. Oertel, M. Hempel, T. Klähn, and S. Typel, “Equations of state for supernovae and compact stars,” *Reviews of Modern Physics*, vol. 89, no. 1, p. 015007, 2017.

[24] E. Annala, T. Gorda, A. Kurkela, and A. Vuorinen, “Gravitational-wave constraints on the neutron-star-matter equation of state,” *Physical review letters*, vol. 120, no. 17, p. 172703, 2018.

[25] F. Sammarruca and T. Ajagbonna, “General features of the stellar matter equation of state from microscopic theory, new maximum-mass constraints, and causality,” *arXiv preprint arXiv:2501.00668*, 2024.

[26] J. R. Oppenheimer and G. M. Volkoff, “On massive neutron cores,” *Physical Review*, vol. 55, no. 4, p. 374, 1939.

[27] Y. Lim and J. W. Holt, “Structure of neutron star crusts from new skyrme effective interactions constrained by chiral effective field theory,” *Physical Review C*, vol. 95, no. 6, p. 065805, 2017.

[28] N. Cruz-Camacho, R. Kumar, M. R. Pelicer, J. Peterson, T. A. Manning, R. Haas, V. Dexheimer, J. Noronha-Hostler, and M. Collaboration, “Phase stability in the three-dimensional open-source code for the chiral mean-field model,” *Physical Review D*, vol. 111, no. 9, p. 094030, 2025.

[29] J. B. Hartle, “Slowly rotating relativistic stars. i. equations of structure,” *Astrophysical Journal*, vol. 150, p. 1005, vol. 150, p. 1005, 1967.

[30] J. B. Hartle and K. S. Thorne, “Slowly rotating relativistic stars. ii. models for neutron stars and supermassive stars,” *Astrophysical Journal*, vol. 153, p. 807, vol. 153, p. 807, 1968.

[31] M. C. Miller, F. Lamb, A. Dittmann, S. Bogdanov, Z. Arzoumanian, K. Gendreau, S. Guillot, W. Ho, J. Lattimer, M. Loewenstein *et al.*, “The radius of psr j0740+ 6620 from nicer and xmm-newton data,” *The Astrophysical Journal Letters*, vol. 918, no. 2, p. L28, 2021.

[32] P. J. Davis, H. Dinh Thi, A. F. Fantina, F. Gulminelli, M. Oertel, and L. Suleiman, “Crust (unified) tool for equation-of-state reconstruction (cuter) v2,” *The European Physical Journal A*, vol. 61, no. 5, p. 120, 2025.

[33] M. Buschmann, C. Dessert, J. W. Foster, A. J. Long, and B. R. Safdi, “Upper Limit on the QCD Axion Mass from Isolated Neutron Star Cooling,” *Phys. Rev. Lett.*, vol. 128, no. 9, p. 091102, 2022.

Appendix A: Sensitivity of the high-density extension to the polytropic and speed-of-sound parameters

This Appendix documents how the high-density continuation adopted in this work depends on the phenomenological parameters entering the (i) intermediate polytropic segment and (ii) the causal speed-of-sound (SoS) continuation. The purpose is twofold: (a) to provide generic guidance on how each parameter affects the equation of state and the resulting mass-radius relation, and (b) to illustrate these trends explicitly through three representative realizations (Sets A-C) shown in Figs. 5 and 6.

Above the density region where microscopic χ EFT calculations are considered reliable, the EoS is extended by matching the β -stable χ EFT EoS to a single polytropic segment in the interval $n_1 \leq n \leq n_2$, followed by a causal SoS continuation for $n \geq n_2$. The intermediate segment is parameterized by:

- the second matching density n_2 , which sets the density at which the SoS construction is activated;
- the adiabatic index Γ_1 , which controls the stiffness of the polytrope and therefore the pressure support at intermediate densities.

Above n_2 , the EoS is generated by integrating the thermodynamic relations using an ansatz for the squared sound speed $c_s^2(n) = dP/d\varepsilon$ that is constrained to be causal and stable, $0 < c_s^2(n) < 1$. The SoS continuation is controlled mainly by:

- a causal cap $c_{s,\text{cap}}^2$, which limits the maximum stiffness at high density;
- a width parameter w_{SoS} , which sets the characteristic density scale over which $c_s^2(n)$ transitions from its matched value at n_2 toward its asymptotic behavior, thereby controlling smoothness and curvature in $P(\varepsilon)$.

In our implementation, the remaining SoS-shape constants are fixed by imposing continuity of c_s^2 and its first derivative at n_2 , ensuring a smooth matching and avoiding artificial kinks at the junction.

To illustrate the parameter dependence, we consider three representative parameter sets (A, B, C) used to generate the EoSs and $M - R$ curves shown in this Appendix. These sets are chosen to probe different stiffness patterns while maintaining thermodynamic consistency and causality. Table III reports the values of the extension parameters.

Figure 5 compares the $P(\varepsilon)$ relations obtained with the three parameter sets. Several generic features emerge.

TABLE III. Representative parameter sets used to assess the sensitivity of the high-density extension. The parameters are: second matching density n_2 , polytropic adiabatic index Γ_1 , SoS width parameter w_{SoS} , and causal cap $c_{s,\text{cap}}^2$.

| Set | n_2 [fm $^{-3}$] | Γ_1 | w_{SoS} [fm $^{-3}$] | $c_{s,\text{cap}}^2$ |
|-----|---------------------|------------|--------------------------------|----------------------|
| A | 0.64 | 3.45 | 0.55 | 0.80 |
| B | 0.60 | 3.30 | 0.45 | 0.90 |
| C | 0.58 | 3.10 | 0.35 | 0.95 |

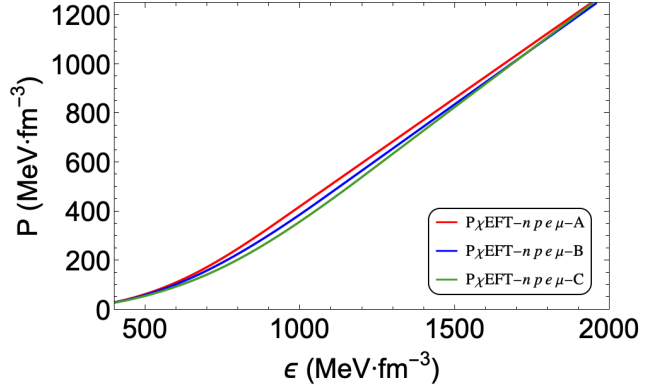


FIG. 5. Sensitivity of the pressure–energy-density relation $P(\varepsilon)$ to the high-density extension parameters. The three curves correspond to the parameter sets in Table III. In the displayed range, Set A (red) is systematically stiffer than Set B (blue), which is stiffer than Set C (green).

a. *Overall stiffness ordering.* Over the displayed range, the three EoSs exhibit a clear ordering in stiffness: Set A (red) yields the largest pressure at fixed energy density, followed by Set B (blue), and Set C (green). This is consistent with the intended design of the sets and demonstrates that moderate variations in the extension parameters produce controlled, monotonic shifts in $P(\varepsilon)$ rather than qualitatively different behavior.

b. *Where parameter sensitivity becomes visible.* At lower ε the curves are close, reflecting the common microscopic χ EFT input and the fact that the extension parameters act only above the matching region. Differences become progressively more pronounced at higher ε , where the intermediate polytrope and then the SoS continuation dominate the pressure build-up.

c. *Interpretation in terms of parameters.* The higher pressure of Set A relative to Set C can be traced to a stiffer intermediate segment (larger Γ_1 and slightly larger n_2) and to an SoS continuation that, despite a lower cap in this particular illustrative choice, transitions smoothly and maintains substantial stiffness across the explored densities. Conversely, the softer Set C corresponds to a smaller Γ_1 and an earlier onset of the SoS continuation (smaller n_2), which together reduce the pressure support at intermediate-to-high densities. The intermediate Set B produces a pressure curve lying between the two and can be viewed as a baseline realization.

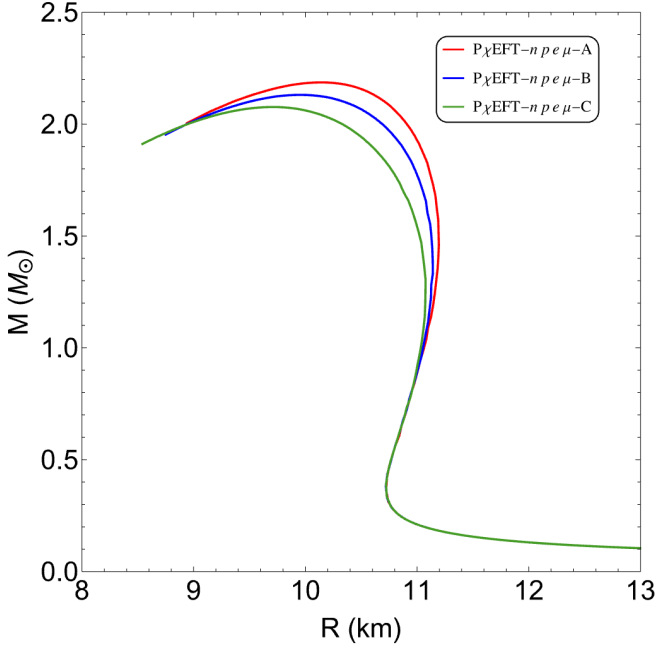


FIG. 6. Mass–radius sequences obtained by solving the TOV equations with the three EoSs shown in Fig. 5. The ordering in stiffness is reflected in the maximum mass and in the behavior near the turning point. For completeness, the full sequences are displayed, including the unstable branch beyond M_{\max} .

Figure 6 shows the $M - R$ sequences resulting from integrating the Tolman–Oppenheimer–Volkoff equations with the three EoSs. The ordering observed in $P(\varepsilon)$ translates into systematic trends in the stellar properties.

d. Maximum mass and high-density stiffness. The maximum mass is primarily controlled by the EoS stiffness at the highest densities reached in the stellar core. In Fig. 6, Set A reaches the largest maximum mass, Set B is intermediate, and Set C yields the smallest maximum mass. This trend is consistent with the EoS ordering in Fig. 5: the larger pressure support at high ε delays the onset of instability and allows heavier configurations.

e. Radii at canonical masses. Radii around canonical masses (e.g. near $1.4 M_{\odot}$) are known to be most

sensitive to the pressure at intermediate densities (a few times saturation). Accordingly, changes in (n_2, Γ_1) influence the horizontal placement of the stable branch. In Fig. 6, the three sequences remain relatively close at low masses (where the common low-density EoS and crust dominate), while differences become visible toward higher masses where the extension parameters increasingly matter.

f. Stable vs. unstable branch. The turning point of each sequence marks the transition from the stable branch ($dM/d\varepsilon_c > 0$) to the unstable branch ($dM/d\varepsilon_c < 0$). In Fig. 6 we display the full sequences, including the unstable part, to highlight how the parameter choices shift the location of the turning point and modify the curvature near the maximum mass. While the unstable branch is not physically realized in isolated neutron stars, its presence in the plot is useful to visualize how the onset of instability depends on the high-density continuation.

The comparison between the sets supports the following generic interpretation:

- (n_2, Γ_1) chiefly regulate the *intermediate-density* stiffness and therefore predominantly affect radii at canonical masses and the overall “horizontal” placement of the stable $M - R$ branch.
- $c_{s,\text{cap}}^2$ primarily controls the *high-density* stiffness and thus the maximum mass and the behavior close to the turning point.
- w_{SoS} mainly controls the smoothness of the transition into the SoS regime; increasing w_{SoS} generally makes $P(\varepsilon)$ smoother and can reduce spurious curvature in $M - R$ arising from overly abrupt matching.

Because different parameter combinations can produce similar $P(\varepsilon)$ over limited density windows, partial degeneracies are expected. For practical tuning, a robust strategy is to first adjust (n_2, Γ_1) to target a desired canonical radius, and then tune $(c_{s,\text{cap}}^2, w_{\text{SoS}})$ to satisfy constraints on the maximum mass while maintaining causality ($c_s^2 < 1$) and stability ($c_s^2 > 0$) across the entire continuation.